

Retention of Nickel and Cobalt in Boda Claystone Formation

Ottó Czömpöly¹, Fruzsina Szabó¹, Margit Fábrián¹ , Tamás Kolonits¹ , Zsolt Fogarassy¹, Dániel Zábó¹ ,
Marc Aertsens² and János Osán^{1,*} 

¹ HUN-REN Centre for Energy Research, Konkoly-Thege M. út 29-33, H-1121 Budapest, Hungary; czompoly.otto@ek.hun-ren.hu (O.C.); szb.fruzsina@gmail.com (F.S.); fabian.margit@ek.hun-ren.hu (M.F.); kolonits.tamas@ek.hun-ren.hu (T.K.); fogarassy.zsolt@ek.hun-ren.hu (Z.F.); zambo.daniel@ek.hun-ren.hu (D.Z.)

² Belgian Nuclear Research Centre (SCK CEN), Boeretang 200, B-2400 Mol, Belgium; marc.aertsens@sckcen.be

* Correspondence: osan.janos@ek.hun-ren.hu

Abstract: The Boda Claystone Formation (BCF) is considered to serve as a natural barrier to the potential high-level radioactive waste repository in Hungary. In order to evaluate the radionuclide retention capacity of the albitic claystone of the BCF, the adsorption and diffusion properties of the rock for Ni²⁺ and Co²⁺ cations (activation products) were investigated separately and in competitive conditions when the two ions were simultaneously added. Batch sorption experiments were performed with powdered and conditioned albitic claystone samples in synthetic pore water to obtain adsorption isotherms. In addition, adsorption tests were performed on petrographic thin sections to check the transferability between dispersed and compact systems. Correlation analysis of microscopic X-ray fluorescence elemental maps recorded on thin sections suggested that nickel is primarily bound to clay minerals (mainly illite and chlorite), which was confirmed by (scanning) transmission electron microscopy measurements. Around illite particles, a newly formed nickel-rich few atomic layer thick phyllosilicate phase was identified. The discrepancy between the experimental and modeled adsorption isotherm at high concentrations could be explained with this nickel-rich new phase. Apart from $C_{in} = 10^{-3}$ M and only Ni²⁺ or Co²⁺ in the source, the apparent diffusion coefficients of Ni²⁺ and Co²⁺ ($C_{in} = 10^{-3}$ – 10^{-2} M) were found to be similar. Overall, the BCF shows promising capabilities to retain the studied radionuclides.



Citation: Czömpöly, O.; Szabó, F.; Fábrián, M.; Kolonits, T.; Fogarassy, Z.; Zábó, D.; Aertsens, M.; Osán, J. Retention of Nickel and Cobalt in Boda Claystone Formation. *Minerals* **2024**, *14*, 1299. <https://doi.org/10.3390/min14121299>

Academic Editor: Tsutomu Sato

Received: 31 October 2024

Revised: 9 December 2024

Accepted: 21 December 2024

Published: 22 December 2024



Copyright: © 2024 by the authors. Licensee MDPI, Basel, Switzerland. This article is an open access article distributed under the terms and conditions of the Creative Commons Attribution (CC BY) license (<https://creativecommons.org/licenses/by/4.0/>).

Keywords: Boda Claystone Formation; nickel retention; clay-rich media; adsorption; diffusion

1. Introduction

To solve the final disposal of high-level radioactive waste (HLW), deep geological repositories will be designed to incorporate a multiple barrier system with engineered and natural components for long-term safety. Over the course of thousands of years, there is a possibility of facilities experiencing leakage. The movement of radioactive elements across natural barriers and their impact on our safety depends on the ability of the released components to be delayed or slowed down. Argillaceous rock formations are regarded as suitable host rocks acting as natural barriers due to their exceptional capacity to retain radionuclide components, primarily because of their high adsorption capability [1,2]. Clay minerals possess negative charges, which are balanced out through the adsorption of cations [3]. This characteristic gives clay minerals a significant cation exchange capacity.

Nickel and cobalt are primarily present as activation products in radioactive waste packages originating from structural elements of reactor vessels. Nickel naturally occurs in five stable (⁵⁸Ni, ⁶⁰Ni, ⁶¹Ni, ⁶²Ni, ⁶⁴Ni) isotopes in the environment. Radioactive nickel isotopes can be linked to human activities, with the most significant being ⁶³Ni, which has a half-life of 100.1 years. Nickel is predominantly present in the +2 oxidation state, which plays a crucial role in the geochemical environment. The present study focuses on the retention of nickel and cobalt, which are considered examples of competitive elements.

In geological systems, cobalt is primarily found in the +2 oxidation state, although the +3 oxidation state is also feasible.

Extensive research has been conducted on the adsorption mechanism of nickel and cobalt onto clay minerals, resulting in the availability of adsorption isotherms, constants, and potentiometric titration data for various minerals. Clay minerals and argillaceous rocks possess a high capacity for sorbing transition metals due to their ion exchange capabilities. However, there has been limited exploration into the reversibility of nickel adsorption on clay minerals. In studies focused on pure mineral systems, such as illite and montmorillonite, newly formed Ni-Al layered double hydroxide has been observed around clay mineral crystallites for liquid phase nickel concentrations above 10^{-4} M, corresponding to 10^{-2} mol/kg Ni in the solid phase [4–7]. The formation of newly formed nickel-rich phyllosilicates on natural argillaceous rock media has not yet been demonstrated.

In Hungary, the Boda Claystone Formation (BCF) [8] is being considered as a candidate host rock for an HLW repository. The BCF shares a similar clay mineral content with other extensively investigated argillaceous formations, like Callovo–Oxfordian (COx) and Opalinus Clay (OPA) [9]. However, the BCF stands out due to its unique characteristics, such as being the oldest formation in Europe (265 Ma) and having an over-consolidated, highly indurated nature with low physical porosity ($\epsilon_{tot} \approx 0.02$) [9,10].

Although, after geological burial, the BCF is situated under a highly reducing environment. Previous studies on radionuclide (RN) migration in the BCF have primarily focused on atmospheric conditions since its early diagenesis took place in an oxidizing environment [5,11–13]. The early diagenesis leads to a high hematite content of BCF albitic claystone, and the majority of clay minerals (illite) also contain Fe as Fe(III) [13,14]. This composition ensures that iron does not oxidize further in atmospheric conditions. For this reason, experiments under atmospheric conditions can provide relevant results for this particular rock system, as demonstrated in recent studies [7].

In the pores of the buffer and backfill materials within radioactive waste repositories, oxygen (O_2) is initially present after construction, gradually decreasing as it is consumed. Additionally, the moisture content in the buffer/backfill may initially be insufficient to fully saturate the entire area. The conditions of the repository environment can be categorized into four possibilities: (i) early-life aerobic and unsaturated conditions, which eventually transition into (ii) saturated conditions. However, during the evolution of the repository, both (iii) unsaturated and (iv) saturated anaerobic conditions can coexist with aerobic phases. Investigating migration under atmospheric conditions can provide valuable insights for performance assessment, particularly concerning the early failure of the repository.

Currently, there have been no published studies focusing on the retention and migration of nickel and cobalt in the competitive environment in the BCF. Therefore, the current research aimed to study the adsorption and diffusion characteristics of the BCF for Ni^{2+} and Co^{2+} under atmospheric conditions, both individually and in competitive environments. This was achieved through the following objectives: (i) assessing the time-dependent nature of adsorption, (ii) examining the adsorption isotherm above 10^{-6} M, (iii) exploring the reversibility of adsorption via isotopic exchange experiments, (iv) identifying the primary minerals responsible for adsorption, (v) comparing adsorption in dispersed and crushed systems, (vi) identifying newly formed phases during uptake, (vii) investigating potential changes in chemical states during adsorption, and (viii) determining apparent diffusion coefficient and rock capacity factor for Ni^{2+} and Co^{2+} using the very same diffusion environment.

2. Materials and Methods

2.1. Sample Origin and Characteristics

The rock under investigation was subjected to geochemical analysis and was obtained as a drilled core sample from the BCF. This formation is situated within the West-Mecsek Mountains of Hungary, specifically in two distinct areas: the Boda Block (BB), characterized by its perianticlinal structure, and the Gorica Block (GB). The sediments within the BCF

exhibit a reddish to red-brown coloration, indicative of the oxidizing conditions in the early diagenetic and depositional environments, as was evidenced before [8,14]. To date, only one reductive interbedding has been identified, spanning a 3–4 m thickness and characterized by a grayish hue and significant pyrite content. The deposition of the BCF occurred approximately 265 million years ago in a shallow-water salt lake environment adjacent to a saline mudflat under arid climatic conditions [15–17]. During sedimentation, the BCF reached the catagenetic stage under high-temperature (200–250 °C) and high-pressure (120–150 MPa) conditions. Subsequently, during the Cretaceous Period, the formation was buried under sediments reaching a thickness of 3.5–4.5 km. This burial and compaction process resulted in the over-consolidation and highly indurated nature of the BCF [9]. The formation is currently situated in a deeply anaerobic subsurface environment at depths exceeding 500 m in some regions. These present-day conditions are distinctly characterized by a highly reducing environment, resulting from geological burial and the complete absence of oxygen infiltration. Factors such as low permeability, high mechanical stability, and minimal fluid movement further contribute to maintaining these reducing conditions, preventing any significant oxidation processes from occurring.

The BCF exhibits a high degree of heterogeneity at both the macro- and microscales. The primary minerals present within it include clay minerals (comprising 10%–55% by mass), authigenic albite (20%–60% by mass), analcime, detrital quartz (5%–30% by mass), carbonate minerals, such as calcite and dolomite (10%–50% by mass), and hematite (5%–10% by mass) [8,18,19]. On a microscale, two notable regions can be highlighted: the predominant clayey matrix and the minor infillings within fractures and vugs. The clayey matrix is primarily composed of albite cement (and analcime cement in the case of GB) along with several clay minerals, predominantly phyllosilicates. These clay minerals include illite (15%–50% by mass), chlorite (0%–35% by mass), smectite, kaolinite, vermiculite, and mixed-structure minerals, which are present in small quantities [8].

For this study, a characteristic core sample of the BCF was selected from BAF-2 borecore deepened in BB at depths of 324.52–324.71 m; its major composition can be found in Table 1 [10]. Trace elemental composition determined by ICP-OES and ICP-MS after digestion with lithium metaborate (LiBO₂) was also reported [10]; the natural background of Co and Ni was 16.3 mg/kg and 46.6 mg/kg, respectively, in the studied core samples. The measured BET surface areas were also reported, both for compact [10] and crushed rocks [20], and were 9.42 m²/g and 14.9 m²/g, respectively.

Table 1. Mineral and chemical composition of the selected BCF core sample expressed as mass percentages (m/m %) [10].

Mineral Composition	(m/m %)	Chemical Composition	(m/m %)
Albite	43	SiO ₂	49.23
Illite	24	Al ₂ O ₃	15.95
Chlorite	6	Fe ₂ O ₃ total	7.83
Vermiculite	2	MgO	4.31
Quartz	7	CaO	4.81
Calcite	5	Na ₂ O	3.14
Dolomite	8	K ₂ O	4.52
K-feldspar	<2	MnO	0.137
Hematite	6	TiO ₂	0.843
Pyrite	<1	CO ₂	4.28
		P ₂ O ₅	0.314
		LOI ¹	8.3
		TOC ²	0.11

¹ LOI: loss of ignition, which refers to the percentage of mass lost after calcination. ² TOC: total organic carbon.

Natural porewater could not be extracted from BCF cores due to its small total porosity ($\epsilon_{tot} = 0.02$). For this reason, a synthetic porewater representative for the BCF was used similarly to the previous studies [5,21,22]. Detailed chemical composition of the synthetic

porewater is given in Supplementary Table S1 [21], which was calculated to be in equilibrium with atmospheric $p\text{CO}_2$ and under the constraint of calcite, dolomite, and quartz saturation with the method described in the study by Bradbury and Baeyens [23]. The main parameters of the porewater are a slightly alkaline pH 8.0 with an ionic strength (I_S) of 3.3×10^{-2} M. Due to the salt-lake origin, the Cl^- and Na^+ content is in the range of 10^{-2} M, which is an order of magnitude lower than those characteristic for argillaceous rocks of marine sediment origin (e.g., Opalinus Clay).

Aqueous speciation was calculated for 10^{-3} M, Ni^{2+} and Co^{2+} were added to the synthetic porewater composition using the PHREEQC Interactive 3.7.3 modeling tool [24] with the ThermoChimie database [25], resulting in the aqueous phase partitioning between ions and chloro, sulphato, and carbonato complex species. Cobalt was calculated to be present as 84.8% Co^{2+} , 4.9% CoSO_4 , 4.6% CoCl^+ , 2.8% $\text{Co}(\text{OH})^+$, 1.5% CoHCO_3^+ , and 1.3% CoCO_3 . For nickel, the calculated partitioning is 89.0% Ni^{2+} , 5.7% $\text{Ni}(\text{SO}_4)$, 1.2% $\text{Ni}(\text{CO}_3)$, 1.5% $\text{Ni}(\text{OH})^+$, 1.6% NiCl^+ , and 0.5% $\text{Ni}(\text{HCO}_3)^+$.

2.2. Adsorption Experiments

The $<63 \mu\text{m}$ fraction of the crushed BCF albitic claystone sample was used for batch adsorption experiments. The powdered sample was preconditioned at $\text{pH } 8.0 \pm 0.1$ with synthetic porewater using the procedure described by Marques Fernandes et al. [5]. To maintain a stable pH, 2 mM of tris(hydroxymethyl)aminomethane (TRIS) was added as a buffer. The concentrations of the major elements, Na, Mg, Cl, K, Ca, Si, and S, in the liquid phases after the conditioning procedure were very similar to the synthetic porewaters.

2.2.1. Adsorption Isotherm Measurements

Batch adsorption experiments were conducted on crushed rock samples under atmospheric conditions to obtain adsorption isotherm. To examine the competitive interaction between Ni^{2+} and Co^{2+} ions, Ni(II) nitrate and Co(II) chloride were added to the synthetic porewater both individually and in combination at varying concentrations. The pH of the solutions was adjusted to 8.0 ± 0.1 after the addition of the metal salts. Experiments with cobalt were only carried out using inactive ^{59}Co in the concentration range of 10^{-6} – 10^{-2} M (initial concentration). Regarding nickel, solutions with 10^{-10} – 10^{-3} M nickel content were prepared, and a part of these solutions was radiolabeled with ^{63}Ni (20 kBq). To study the effect of competition, solutions with concentrations between 10^{-6} M and 10^{-2} M (initial concentrations) for both Co and Ni were prepared. For the determination of concentrations of inactive solutions, ICP-OES was applied; meanwhile, for the ones with radiotracers, liquid scintillation counting (LSC) measurements were performed. During the adsorption experiments, the solid to liquid ratio (m/V) used was 4.2 g/L:0.21 g of crushed and conditioned rock, which was added to the 50 mL solution in 100 mL shaker vessels. The suspensions were shaken on an orbital shaker for 28 days. After this time period, the suspensions were filtered using syringe filters (220 nm, cellulose–acetate), and aliquots were analyzed. Adsorption onto the shaker vessel walls was found to be below 1% and neglected for further calculations. The results are presented as the distribution coefficient (R_d), and the adsorbed ion concentration (C_{sorb}) calculated as $R_d = (C_{\text{in}} - C_{\text{eq}})/C_{\text{eq}} \cdot (V/m)$ and $C_{\text{sorb}} = (C_{\text{in}} - C_{\text{eq}}) \cdot (V/m)$, where C_{in} and C_{eq} denote the initial and equilibrium concentrations (mol/L), respectively. V is the volume of the solution (mL) and m is the mass of the solid phase (g). Uncertainties of R_d and C_{sorb} were calculated using error propagation as described in the work by Orucoglu et al. [26]. Relative uncertainties associated with C_{in} and C_{eq} were considered as 10% in the whole concentration regime for LSC and 15%, 10%, and 7% in the $<10^{-7}$ M, 10^{-7} – 10^{-3} M, and $>10^{-3}$ M concentration range for ICP-OES. Uncertainties of the solid to liquid ratio (m/V) were considered negligible. The batch adsorption experiments were carried out in duplicate.

For both $\text{Ni}(\text{OH})_2$ and $\text{Co}(\text{OH})_2$, the solubility limit is around 5×10^{-3} M in the current conditions. To ensure the stability of the high-concentration solutions utilized in our experiments, rigorous checks were conducted employing various analytical techniques. Initially,

the 10^{-3} – 10^{-2} M solutions were analyzed using ICP-OES both before and after filtration through a 220 nm syringe filter. No significant change in the concentration of the solutions was observed, indicating the absence of any precipitates or alterations in the solution composition following filtration. Subsequently, the solutions underwent ultracentrifugation at $15,000 \times g$ for 30 min. Following centrifugation, the concentration of the solutions was re-evaluated. No decrease in concentration or presence of sedimentation was detected, further corroborating the stability of the solutions under high centrifugal forces. Dynamic Light Scattering (DLS) was employed to assess the size distribution and stability of particles within the solutions both before and after ultracentrifugation. DLS analysis revealed no discernible change in the spectra of the solutions, indicating that no particles above the system background were detected, which remained consistent throughout the centrifugation process. Collectively, these stability assessments utilizing ICP-OES, ultracentrifugation, and DLS confirm the robustness and integrity of the high-concentration solutions utilized in our experiments. The absence of changes in concentration, sedimentation, or alterations in particle size distribution underscores the reliability of our experimental conditions and the validity of the subsequent data analysis. Equilibrium models, such as those employed in geochemical calculations, often forecast precipitation phenomena at higher Ni and Co concentrations ranging from 10^{-3} to 10^{-2} M. However, it is essential to recognize the underlying assumptions and limitations of these models. It is noteworthy that the experimental conditions and duration of our study may not fully align with the timescales considered in equilibrium models. While these models predict precipitation under idealized conditions, the actual kinetics of precipitation reactions may differ significantly, particularly within the timeframe of our experiments.

2.2.2. Isotopic Exchange Experiments

To investigate the Ni adsorption reversibility, suspensions were prepared by adding 0.21 g powdered and conditioned claystone to 50 mL solutions containing nickel at varying concentrations ranging from 10^{-10} to 10^{-3} M. After a shaking period of 31 days, 5 mL aliquots taken from the suspensions were filtered through a 220 nm cellulose–acetate syringe filter. ICP-OES was applied to measure the concentration of nickel. Below the minimum detectable concentration of $10 \mu\text{g/L}$ (ca. 1.7×10^{-7} M), R_d values were taken from the adsorption isotherm reported in a previous study applying LSC [27], and the equilibrium concentrations were calculated using those R_d values.

Subsequently, the remaining 45 mL suspensions were radiolabeled with 50 kBq of $^{63}\text{NiCl}_2$. Immediately after radiolabeling, a 5 mL initial sample was taken and filtered again using 220 nm cellulose–acetate syringe filters. The labeled suspensions were shaken for 30 days. The activity of ^{63}Ni was measured using liquid scintillation counting (LSC) in the filtered liquid phases from both the initial solutions and those shaken for 30 days (with ^{63}Ni). Reversibility was determined through a comparison of adsorbed fractions of inactive and active nickel, following an approach reported by Rahman et al. [28]. The adsorbed fraction was calculated as $f_{ads} = (C_{in} - C_{eq})/C_{in}$, the exchanged fraction was $f_{exch} = (A_{in} - A_{eq})/A_{in}$, and the reversible fraction was $f_{rev} = f_{exch}/f_{ads}$, where A_{in} and A_{eq} denote the initial and equilibrium activity of ^{63}Ni . The isotopic exchange experiments were carried out in triplicate.

2.2.3. Adsorption Experiments on Petrographic Thin Sections

High-purity silicon wafers were used as substrates for the preparation of petrographic thin sections. Pre-selected small pieces of BCF core samples were fixed onto quartz glass slides by beeswax. Approximately 1 mm sections were cut using a low-speed saw (Buehler IsoMet) and then ground to a thickness of $\approx 50 \mu\text{m}$. A $20 \times 20 \text{ mm}^2$, $380 \mu\text{m}$ thick Si holder was fixed onto the ground sample surface using epoxy resin. The sample was then reheated to melt the beeswax to detach the Si wafer with the thin section from the glass slide. The sample surfaces were then polished using $0.25 \mu\text{m}$ diamond paste.

The Si wafers were positioned individually in 100 mL polypropylene (PP) beakers and secured by custom-made PTFE holders keeping the thin sections facing upwards. Each beaker contained 50 mL of a synthetic porewater solution containing Ni^{2+} and/or Co^{2+} at concentrations ranging from 10^{-5} to 10^{-2} M. Identical synthetic porewater solutions were used in adsorption experiments involving thin sections or powdered rock samples. Initially, the liquid phase remained stationary, but later, a magnetic stirrer was applied in an incubator to maintain circulation at a constant temperature of 20 °C.

2.2.4. Microscopic XRF Measurements

Petrographic thin sections were analyzed using a custom-built laboratory μ -XRF setup, enabling point analysis and elemental mapping [12]. The system comprises a low-power X-ray tube with Rh anode and a polycapillary optics (IfG, Berlin, Germany) that generates a 20 μm X-ray beam. A 30 mm^2 active area Si drift detector (SDD) with Peltier cooling (KETEK, Munich, Germany) was employed to detect the emitted characteristic X-rays. Two-dimensional scanning is achieved by moving the sample across a fixed X-ray microbeam. The measurement process is computer controlled via custom LabView-based software developed specifically for the system [12]. This software controls the sample stage, spectral acquisition, and optical imaging of the sample. Additionally, μ -XRF using a synchrotron radiation source was conducted at the mySpot beamline of Bessy-II (Berlin, Germany) [29]. A 20 μm microbeam formed by polycapillary optics was used for measurements of thin sections in a $45^\circ/45^\circ$ geometry utilizing an SDD with a 100 mm^2 active area for the detection of X-rays. Representative regions of a few mm^2 were selected on thin sections for 2D elemental mapping by means of laboratory and synchrotron-radiation μ -XRF. Sum spectra collected over the entire measured regions served as a basis for the quantification of adsorbed (Ni, Co) and major rock-forming elements. PyMCA software was used for spectrum evaluation. The base consideration for the calculations was the known Fe content of the sample and measured relative sensitivities using a multi-elemental standard reference material.

2.2.5. TEM Measurements

Dedicated samples for TEM investigations were prepared in duplicate by the addition of 0.21 g ground and conditioned claystone to 50 mL of the synthetic porewater solution with 10^{-3} M Ni in 100 mL vessels. To achieve equilibrium, the suspensions were agitated for 28 days. After agitation, they were centrifuged at 1100 rcf for 5 min, keeping the supernatant on top. The supernatant was decanted immediately prior to TEM investigations, and 20 mL of Type-I water (resistivity greater than 18.2 $\text{M}\Omega\text{cm}$) was added to the beakers. The settled particulates were resuspended using an ultrasonic bath. A 30 μL aliquot was dropped onto a copper TEM grid with a lacey carbon film coating and dried for 3 h under infrared light. The (scanning) transmission electron microscope ((S)TEM) measurement was carried out using a Themis 200 Cs corrected (S)TEM. The microscope point resolution is approximately 0.07 nm in High-Resolution Transmission Electron Microscope (HRTEM) mode. The microscope was operated at 200 kV. Elemental maps were taken with Super-X EDX detectors in STEM mode.

2.2.6. XAS Measurements

X-ray absorption near-edge structure (XANES) spectroscopy analyses were conducted at the Elettra synchrotron facility in Trieste, Italy. These measurements were carried out on both pressed pellets and thin sections at the XRF beamline. The focusing optics in this set up produced a relatively large beam, approximately $500 \times 300 \mu\text{m}^2$ in size (horizontally \times vertically). The beam size could be further reduced by employing exit slits. Si(111) monochromators were utilized for XANES measurements [30].

While the entire beam was utilized for pressed pellets, a beam of $50 \times 50 \mu\text{m}^2$ with an illumination at 1° was employed for the measurement of thin sections. At selected points XANES measurements were performed to study the possible oxidation state changes, both

in the case of Ni and Co. XANES measurements were performed on samples treated with $C_{in} = 10^{-3}$ M Ni and Co. The samples are crushed rock filtered after the batch adsorption experiment, pressed into pellets, and then vacuum sealed. The binder material of the pellets is polyvinylpyrrolidone, and they contain 1% of the element of interest.

The purpose of conducting XANES experiments was to determine whether salt precipitation occurred (by examining the chemical form of the adsorbed metals) from the porewater and to identify any potential changes in chemical states during the formation of secondary phases.

2.3. Through-Diffusion Experiments

2.3.1. Experimental Set Up

For the through-diffusion study, polycarbonate diffusion cells were employed, as described by [11]. The cells featured a claystone section that partitioned into two compartments, an upstream reservoir and a downstream reservoir, each with a volume of 165 mL. For through-diffusion experiments, slices with thickness between 3 and 6 mm were cut from 62 mm diameter core samples. The clay cross-section in the cell is 12.57 cm^2 (diameter 4 cm). To assemble the cell, the claystone slice was affixed, and the two sides were securely fastened together. Because of the minimal swelling of Boda Claystone, the diffusion cells were used without filters. To saturate the BCF core disc, both upstream and downstream reservoirs were filled with synthetic porewater. Over the course of a 42-day conditioning period, the solutions were replaced every 2 days.

After conditioning, the solution containing the elements of interest was introduced into the upstream reservoirs of each diffusion cell. Three different variations of the upstream solutions were prepared, each at two different concentrations (all together, there were 6 cells). These 6 cells consist of the following:

- Two cells with only Ni: Ni-2 and Ni-3 (initial concentration of 10^{-2} M and 10^{-3} M);
- Two cells with only Co: Co-2 and Co-3 (10^{-2} M and 10^{-3} M);
- Two cells with Ni and Co combined, both with the same initial concentration: CoNi-2 (10^{-2} M) and CoNi-3 (10^{-3} M).

The diffusion of each species can be regarded as mutually independent, allowing for a direct comparison of the diffusion characteristics of Ni and Co under identical conditions. Both the upstream and downstream reservoirs were refreshed on a regular basis with the prepared upstream solutions and porewater, respectively. Monitoring of the concentration changes was performed using ICP-OES and TXRF. The duration of the experiments was approximately 100 days.

2.3.2. Modeling

As in all clays, in Boda Claystone, two parameters are needed to predict the diffusion behavior: the apparent diffusion coefficient D_{app} (m^2/s) and the rock capacity α (-). For retarded species, like Ni^{2+} and Co^{2+} , the rock capacity α is related to the distribution coefficient R_d (m^3/kg) by $\alpha = \varepsilon + \rho R_d \approx \rho R_d$, with $\varepsilon_{tot} = 0.02$ as the total Boda Claystone porosity (-) and $\rho = 2700\text{--}2800 \text{ kg}/\text{m}^3$ as the dry bulk density. The effective diffusion coefficient D_{eff} (m^2/s) can be calculated as $D_{eff} = \alpha D_{app}$.

For modeling, the diffusion equation is solved numerically by COMSOL coupled with MATLAB for optimization. The existing VC-CC (Variable Concentration at the upstream reservoir and Constant Concentration at the downstream reservoir [31]) model was used with a large upstream volume $V_{up} = 1000 \text{ cm}^3$ (with a cross-section $S = 12.57 \text{ cm}^2$, the ratio $V_{up}/S \approx 80 \text{ cm} \gg$ the clay core length) to assure an approximately constant concentration at the upstream reservoir. The downstream (outlet) concentration was fitted as a function of time.

3. Results and Discussion

3.1. Adsorption Results

3.1.1. Adsorption Isotherm

Figure 1 shows similar adsorption isotherms for Ni(II) and Co(II) when either of the ions were present alone in the liquid phase during adsorption experiments, with R_d values for both elements falling within the uncertainty ranges. However, in competitive conditions, the adsorption is significantly lower (based on one side t-probe) than in unique systems. In the high concentration range (10^{-4} – 10^{-2} M) where the complexation sites are fully saturated and ion exchange becomes the primary adsorption mechanism, Ni generally shows higher R_d values than Co, though the large errors at 10^{-3} and 10^{-2} M C_{eq} make this difference less definitive. In contrast, in the 10^{-6} – 10^{-4} M range, where adsorption occurs through surface complexation at the weak sites, the R_d values for cobalt surpass those of nickel and approach the values obtained under non-competitive conditions (though they are still half order of magnitude lower). This means that there is a competition effect of Co on Ni sorption between 10^{-6} and 10^{-4} M, but not above 10^{-4} M, while the effect of Ni on Co sorption is only visible above 10^{-3} M and not below.

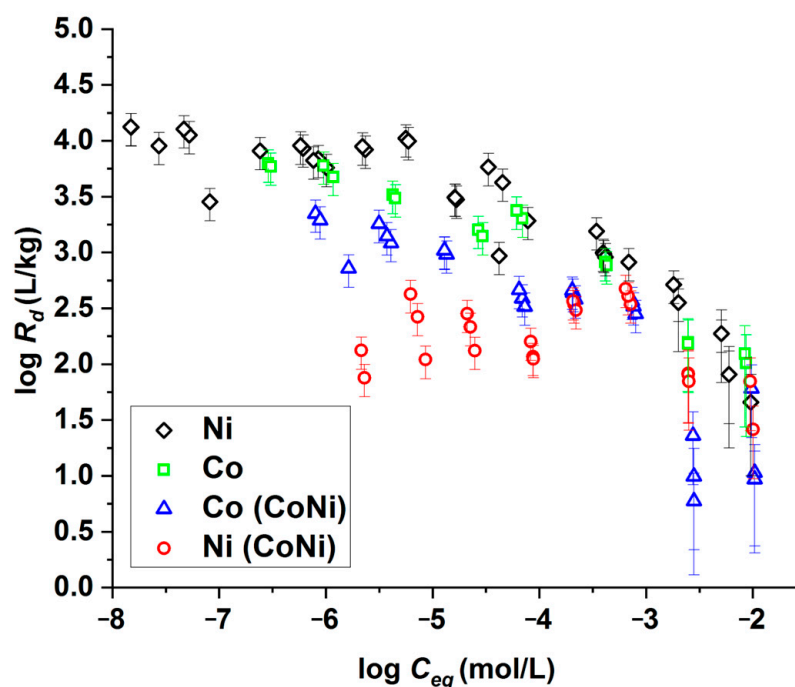


Figure 1. Adsorption isotherm of Ni and Co on the BCF at pH 8.0, as represented by the distribution coefficient (R_d). The terms Co and Ni indicate data collected when each ion was present separately, whereas Co (CoNi) and Ni (CoNi) represent the results obtained under competitive conditions, where both ions were added at the same concentration. The error bar is derived from the consistency of the batch experiments using error propagation, indicating a $k = 2$ confidence level (95% confidence interval).

By comparing Ni adsorption isotherms for different argillaceous rocks conducted in the respective porewater conditions (Figure 2), R_d shows a similar trend in the BCF as in OPA in the 10^{-9} – 10^{-4} M concentration range, with R_d values in the same order of magnitude. A drop in R_d at high Ni concentrations was also observed in COx [32], and the generally lower R_d values can be explained by the difference in porewater chemistry (lower pH) and in the clay mineral composition.

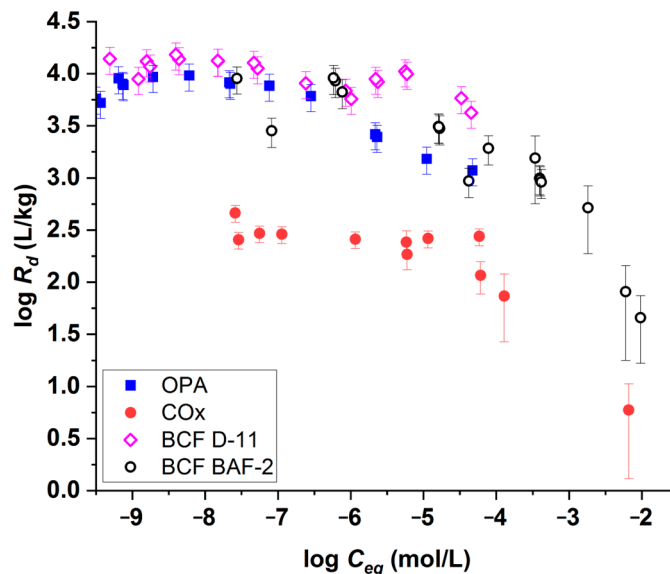


Figure 2. Ni adsorption isotherms for different argillaceous rock systems with the respective porewater conditions: Opalinus Clay (OPA) IS = 2.3×10^{-1} M, pH 7.8 [5]; Callovo–Oxfordian Clay (COx) IS = 5.7×10^{-2} M, pH 7.4 [6], BCF D-11 [27]; and BCF BAF-2 (present study) IS = 3.3×10^{-2} M, pH 8.0.

3.1.2. Reversibility of the Adsorption

The reversibility of Ni adsorption was also investigated through isotopic exchange experiments by introducing a ^{63}Ni radiotracer while maintaining equilibrium conditions. Surface complexation of metals on clay minerals can generally be described in terms of the uptake on sets of strong and weak sorption sites, where the latter can be considered as amphoteric edge sites. Strong sites have a much smaller capacity but form considerably stronger complexes with metals and dominate the adsorption at the trace concentration regime [32]. The availability of strong adsorption sites and new phase formations influence the obtained exchangeable fraction. The highest observed reversibility was 0.7, which can be attributed to the presence of strong sorption sites (Table 2). The strong sites of illite become saturated at $C_{eq} \approx 10^{-7}$ [5], and the weak sites begin to dominate, which leads to an expectation that adsorption reversibility will increase with higher concentrations. However, the reduction in reversibility can be attributed to new phase formation, resulting in a low reversibility of 0.27 for the highest studied concentration $C_{eq} = 4 \times 10^{-4}$ M (Table 2).

Table 2. Adsorbed (f_{ads}), exchanged (f_{exch}), and reversible (f_{rev}) fraction resulting from isotope exchange experiments in equilibrium conditions using the ^{63}Ni radiotracer. The standard deviation of the fractions was found to be 0.03.

C_{eq} (M)	8.6×10^{-12}	5.8×10^{-11}	4.9×10^{-10}	5.6×10^{-9}	5.3×10^{-8}	6.5×10^{-7}	1.6×10^{-5}	4.0×10^{-4}
f_{ads} (-)	0.91	0.94	0.95	0.94	0.95	0.92	0.81	0.56
f_{exch} (-)	0.64	0.60	0.47	0.56	0.61	0.55	0.38	0.15
f_{rev} (-)	0.70	0.64	0.50	0.60	0.65	0.60	0.47	0.27

3.1.3. Lateral Distribution and Correlation of Adsorbed Co and Ni and Rock-Forming Elements

Laboratory micro-XRF elemental mapping was performed on a BCF thin section treated with synthetic porewater containing both Ni(II) and Co(II) ions at $C_{in} = 5 \times 10^{-2}$ M. A $1.00 \times 0.75 \text{ mm}^2$ area was mapped with 25 μm steps and a 150 s counting time per pixel. Table 3 displays the correlation matrix (based on 1189 points, 41×29 points map) between the primary rock-forming elements and adsorbed species. Supplementary Figure S1 shows the elemental maps and Supplementary Figure S2 shows the scatter plots of the correlation study. Based on the calculation of the correlation coefficients, with a significance test, we

can assume that there is a strong ($r > 0.6$) and significant ($p < 0.05$) correlation between S/Cu, Ni/Co, Co/Ni, K/Ni, and Fe/Ni. The high Co/Ni correlation coefficient ($r = 0.96$) emphasizes that the uptake mechanism of Co(II) and Ni(II) is similar in the studied BCF albitic claystone. The strong correlation of K/Ni and Fe/Ni implies that Ni uptake occurred in minerals that contain both K and Fe elements. Although the Fe/Co correlation coefficient is somewhat lower, these minerals are also predominant for Co uptake. In the BCF albitic claystone, illite emerges as the predominant mineral with the concurrent presence of Fe and K, implying that illite, alongside clay minerals, plays a significant role in adsorption. The moderate correlation between K and Fe ($r = 0.54$), however, indicates that potassium and iron may exist not only in clay minerals but also in other phases, like K-feldspar and hematite.

Table 3. Correlation coefficients ($p < 0.05$) between rock-forming elements and adsorbed species (Co and Ni). Correlation coefficients greater than 0.6 are highlighted in bold.

	Ca	S	Cu	Fe	K	Co	Ni	Ti	Si
Ca	1.00	−0.18	−0.16	0.19	0.29	0.38	0.38	0.25	−0.28
S	−0.18	1.00	0.97	0.48	−0.21	−0.38	−0.26	−0.19	−0.25
Cu	−0.16	0.97	1.00	0.50	−0.19	−0.34	−0.24	−0.17	−0.25
Fe	0.19	0.48	0.50	1.00	0.54	0.52	0.61	0.35	−0.61
K	0.29	−0.21	−0.19	0.54	1.00	0.71	0.72	0.39	−0.50
Co	0.38	−0.38	−0.34	0.52	0.71	1.00	0.96	0.46	−0.42
Ni	0.38	−0.26	−0.24	0.61	0.72	0.96	1.00	0.45	−0.46
Ti	0.25	−0.19	−0.17	0.35	0.39	0.46	0.45	1.00	−0.28
Si	−0.28	−0.25	−0.25	−0.61	−0.50	−0.42	−0.46	−0.28	1.00

3.1.4. Transferability of the Results Between Compacted and Dispersed Systems

It is essential to determine whether sorption phenomena observed in dispersed systems with powdered rocks are applicable to compacted systems that maintain the integrity of clay-rich rocks. Petrographic thin sections are typically used for microspectrometry investigations, which allow the mineral phase distribution to be examined in quasi-intact rocks. Consequently, the transferability was investigated on BCF thin sections, comparing the results to those obtained for crushed rock samples treated with Ni(II) cations.

Figure 3 summarizes the results, showing the amount of Ni sorbed (panel a) and the distribution coefficient R_d (panel b). In relation to adsorption experiments involving dispersed systems, our current findings utilizing inactive nickel and ICP-OES are in good agreement with the previous results obtained using the ^{63}Ni radiotracer and LSC [5]. The R_d values gradually decreased for concentrations above 10^{-5} M from approximately 10^4 L/kg to around 30 L/kg within the concentration range extended to 10^{-2} M.

In the case of thin sections, the equilibrium concentration was calculated based on the amount of nickel adsorbed by the solid phase, which was obtained using the micro-XRF method. This indirect method was necessary due to the small differences between the initial and equilibrium concentrations caused by the high liquid to solid (L/S) ratio (approximately 1500 L/kg). The error bars in Figure 3 reflect the lower accuracy associated with these indirectly determined concentrations.

Maintaining the porewater solution without circulation, the adsorbed amount of Ni for thin sections was an order of magnitude lower than predicted from the adsorption isotherm obtained for crushed rock samples (Figure 3). This should also be considered for the evaluation of diffusion experiments conducted without liquid phase circulation. In contrast, conventional batch experiments with crushed rock samples keep the suspensions continuously shaken. Therefore, the circulation of the porewater solution was enforced by a magnetic stirrer for the additional adsorption experiments with thin sections. With the porewater solution in circulation (represented by solid squares in Figure 3), the agreement between thin sections and crushed rock samples improved significantly. For moderate concentrations (8×10^{-5} M), the R_d and C_{sorb} values for Ni aligned well for thin sections

and crushed rock samples, but for high concentrations (10^{-3} M), the values obtained for thin sections were lower than anticipated, as they were similar to those without circulation.

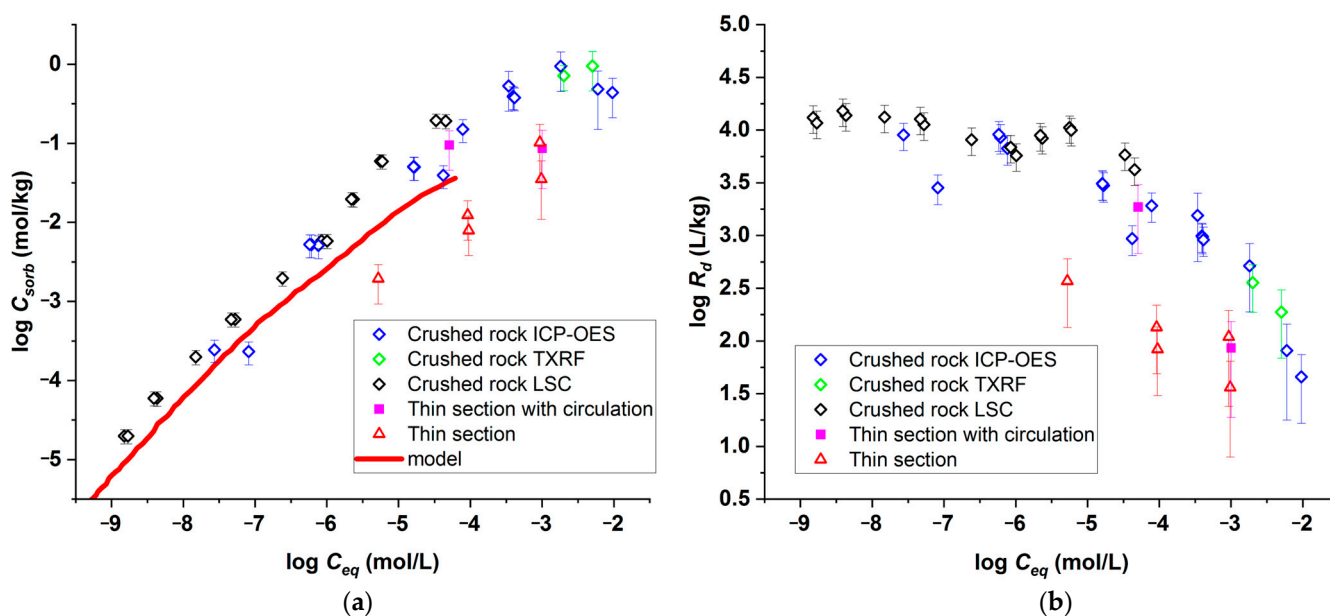


Figure 3. Ni adsorption isotherm for the BCF obtained from various experimental setups. The adsorbed amount (C_{sorb}) (a) and distribution coefficient (R_d) (b) are plotted against the equilibrium concentration (C_{eq}). The terms ICP-OES, TXRF, and LSC refer to the analytical method used for batch experiments conducted with crushed claystone samples. Crushed rock LSC data points and model curves were reproduced from the study by V er et al. [27].

As the surface area for compact rock ($9.42 \text{ m}^2/\text{g}$) is significantly lower than that of crushed rock ($14.9 \text{ m}^2/\text{g}$), the adsorbed amount can be normalized to the surface area instead of mass. The adsorbed amount values for thin sections would scale with a factor of 1.6, resulting in an increase of 0.2 on the logarithmic scale, slightly improving the agreement between the results for thin sections and crushed rocks.

3.1.5. Identification of Irreversibly Formed Phases

TEM and EDS analyses were conducted on individual crystallites selected from suspensions treated with Ni ($C_{in} = 10^{-3}$ M) and compared to untreated samples. Consistent with the initial assumptions, Ni uptake could only be associated with clay minerals typical of the BCF, specifically illite and chlorite (Figure 4). Based on the respective interlayer distances of 10 \AA and 14 \AA , illite and chlorite crystallites could be readily distinguished. EDS elemental mapping revealed a high enrichment of nickel at the edge of clay mineral crystallites (Figure 4d), where the nickel content even exceeded that of iron, reaching twice the iron concentration (Table 4, Area #2). The concentration of other major components (Mg, Al, Si) in the nickel enrichment deviated from that of illite. Regarding the center of the illite crystallite, where adsorption was the main mechanism of Ni uptake, Ni content was elevated but below that of Fe (Table 4, Area #3). TEM measurements were also performed around non-clay minerals, and no formation of secondary phases or areas enriched in Ni were observed around rutile, hematite, and albite crystallites. Untreated samples were also investigated, and no Ni phases were identified around the particles. The formation of a new phase as an important mechanism of Ni uptake was confirmed with TEM and EDS analyses of BCF samples; however, further investigation is required for its unequivocal identification. The formation of phyllosilicates was demonstrated before in pure mineral systems [33,34]; however, these results show their occurrence in clay-rich rock media for the first time.

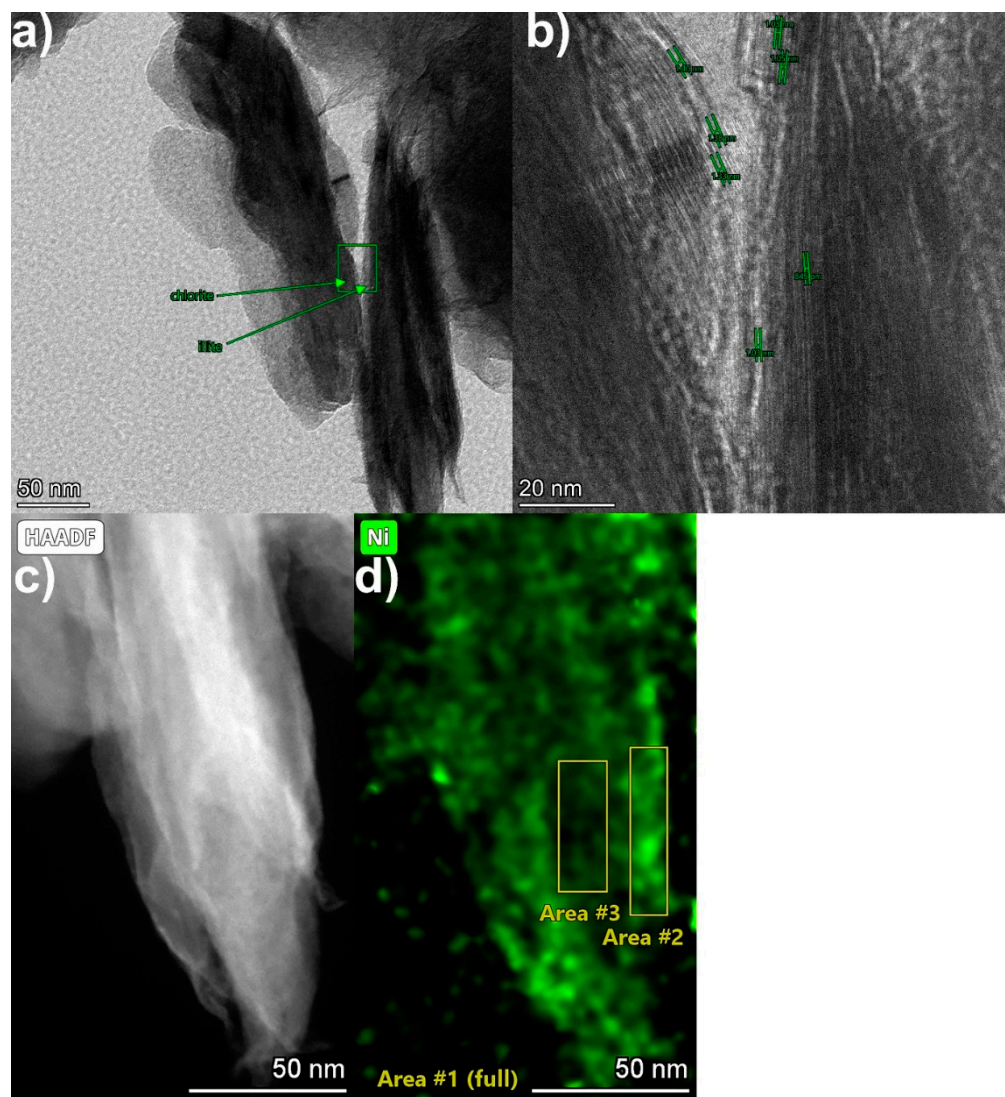


Figure 4. TEM/EDS results for clay mineral crystallites after treatment with Ni ($C_{in} = 10^{-3}$ M). The bright-field (BF) TEM image in panel (a) shows overlapping particles, while the high-resolution TEM image in panel (b) displays the overlay with visible lattice spacings, based on which chlorite (left) and illite (right) crystallites could be distinguished. Panel (c) presents a high-angle annular dark-field (HAADF) STEM image, and panel (d) shows the EDS nickel elemental map of the region surrounding the illite crystallite.

Table 4. EDS elemental composition of three areas of the analyzed region highlighted in Figure 4d. Area #1 (full), entire analyzed region; Area #2, nickel enrichment surrounding the illite crystallite; Area #3, inside the illite crystallite after Ni treatment.

Element	Area 1 [at.%]	Area 2 [at.%]	Area 3 [at.%]
O	57.92 ± 2.07	56.4 ± 1.96	55.69 ± 2.11
Na		1.35 ± 0.36	1.17 ± 0.17
Mg	6.57 ± 1.25	4.36 ± 0.88	9.31 ± 1.72
Al	9.19 ± 1.68	7.87 ± 1.47	9.7 ± 1.77
Si	13.07 ± 2.21	11.18 ± 1.95	12.16 ± 2.09
Cl	0.36 ± 0.07	0.62 ± 0.19	0.21 ± 0.09
K	1.04 ± 0.18	1.1 ± 0.26	0.69 ± 0.15
Ca	0.24 ± 0.03	0.41 ± 0.12	0.23 ± 0.06
Fe	5.52 ± 0.72	5.16 ± 0.70	6.93 ± 0.90
Ni	6.09 ± 0.87	11.55 ± 1.56	3.92 ± 0.58

3.1.6. Chemical State of Adsorbed Co and Ni

XANES spectra of the samples both in the form of pressed pellets and thin sections are compared to the spectra of reference compounds (Figure 5) in order to gain insight into the chemical state of adsorbed metals. No significant differences could be observed either between pressed pellets (powdered form) and thin sections treated with the same element or between samples treated with Co^{2+} or Ni^{2+} alone or treated with both Co^{2+} and Ni^{2+} ions. Although the possibility of redox reactions during the secondary phase formation cannot be excluded for cobalt, no change in the oxidation state could be identified.

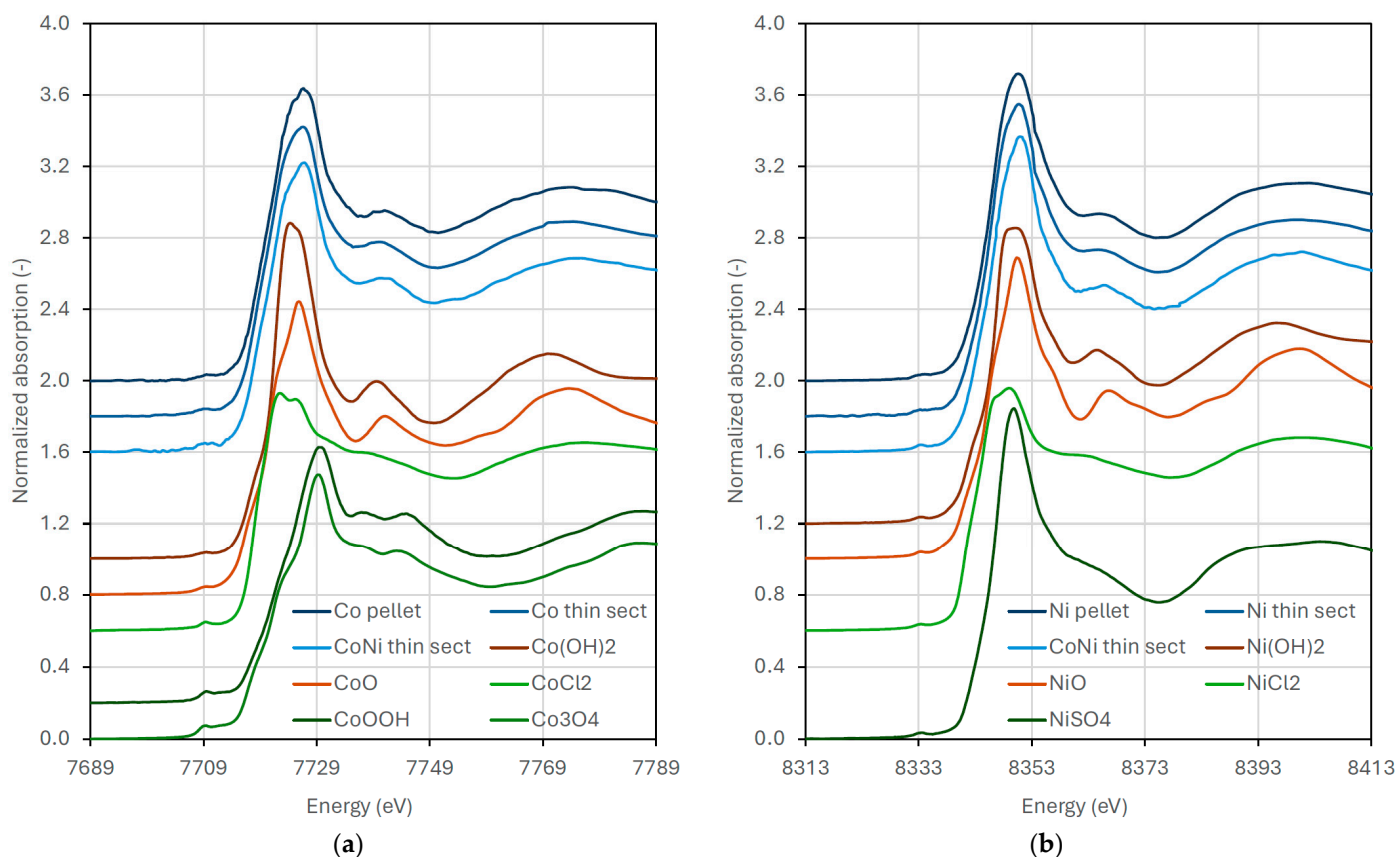


Figure 5. Ni-K (a) and Co-K (b) XANES spectra of pressed pellet (powdered) and thin section samples treated with Co and Ni at initial concentrations of 10^{-3} M. CoNi indicates the data for the sample treated with both ions. Spectra of reference compounds are also presented for comparison.

3.2. Results of the Through-Diffusion Experiments

The results of the modeling of Ni^{2+} and Co^{2+} diffusion are summarized in Table 5, both separately and in competitive conditions. Details of the modeling results are presented in Supplementary Figure S3. For both ions, the apparent diffusion coefficients are higher, and the rock capacity factors are smaller for higher initial concentrations. A lower D_{app} corresponds to a higher rock capacity factor α . At a high initial concentration of 10^{-2} M, the D_{app} values for the two studies ions are not significantly different. However, at $C_{in} = 10^{-3}$ M, Ni^{2+} has a higher apparent diffusion coefficient than Co^{2+} , although the difference is smaller than the uncertainty in competitive conditions. A higher Ni^{2+} apparent diffusion coefficient than Co^{2+} is in line with the higher affinity for Co^{2+} shown with the fitting of the adsorption isotherm. From the rock capacity factor α , the R_d values were calculated and compared to the batch adsorption isotherm data. The R_d values derived in this way tend to be lower than the ones obtained from the batch adsorption experiment. However, as shown in Chapter 3.1.5 (results of transferability from compacted to diluted systems), in compacted systems,

R_d is lower by one order of magnitude at the same concentration (without circulation of the liquid phase).

Table 5. Results of the modeling of the through-diffusion experiments. The apparent diffusion coefficient D_{app} and the capacity factor α are fitted parameters, while R_d is calculated from the capacity factor ($R_d \approx \alpha/\rho$).

Cell Name	Clay Core Length L (mm)	C_{in} (Ni) (mol/L)	C_{in} (Co) (mol/L)	Species	D_{app} (10^{-13} m ² /s)	α (-)	R_d (L/kg)
Ni-2	3.9	10^{-2}	–	Ni ²⁺	5.6 ± 0.9	2.5 ± 0.6	0.9
CoNi-2	5.5	10^{-2}	10^{-2}	Ni ²⁺	5.2 ± 0.4	1.5 ± 0.3	0.6
CoNi-2	5.5	10^{-2}	10^{-2}	Co ²⁺	5.1 ± 0.4	1.7 ± 0.3	0.6
Co-2	5.78	–	10^{-2}	Co ²⁺	5.1 ± 0.4	3.4 ± 0.5	1.2
Ni-3	5.48	10^{-3}	–	Ni ²⁺	4.5 ± 0.4	9.5 ± 2.5	3.5
CoNi-3	3.425	10^{-3}	10^{-3}	Ni ²⁺	3.1 ± 0.4	7.7 ± 1.3	2.8
CoNi-3	3.425	10^{-3}	10^{-3}	Co ²⁺	2.7 ± 0.3	9.2 ± 1.5	3.3
Co-3	4.45	–	10^{-3}	Co ²⁺	2.0 ± 0.1	28.2 ± 4.0	10.3

Christiansen and Torstenfelt [35] presented two D_{app} coefficients for nickel in loosely compacted bentonite, proposing the existence of two species during transport. Their calculations were based on the diffusion profile within the rock, where they postulated two mechanisms. Near the surface, where the nickel concentration in the porewater was higher, they assumed the precipitation of Ni(OH)₂. Beyond a certain point, where the nickel concentration fell below the solubility limit of Ni(OH)₂, nickel transport occurred in the form of Ni²⁺. The corresponding D_{app} values were reported as 7.7×10^{-13} m²/s and 9.6×10^{-12} m²/s, respectively.

Garcia-Gutierrez et al. [36] studied the diffusion of ⁶⁰Co in compacted bentonite. They performed calculations using analytical and numerical solutions and received D_{app} for Co in the range of 0.5 – 2.3×10^{-13} m²/s. However, they stated that they cannot accurately replicate the experimental data using a constant D_{app} value in the modeling, as D_{app} tends to rise with increasing distance from the source.

Garcia-Gutierrez et al. [37] also investigated the diffusion of ⁶⁰Co in the Opalinus Clay with in-diffusion experiments. The D_{app} obtained via an analytical solution was 2.4 – 3.5×10^{-14} m²/s for a low initial concentration of 3.5×10^{-8} M. As we observed a decreasing trend of D_{app} with decreasing Co²⁺ initial concentrations, our results indicate that the diffusion parameters for the BCF for Co²⁺ are expected to be similar to those obtained for Opalinus Clay.

The aim of the diffusion experiments in this study was to compare the values obtained for Ni and Co under similar conditions. Even though the initial concentrations of Co and Ni were very high, the obtained diffusion coefficients for the BCF are in the same order of magnitude as the previously reported values for other rock formations.

4. Conclusions

This study investigated the adsorption of Co(II) and Ni(II) on a clay-rich rock (BCF) through batch and thin-section experiments. Most adsorption occurs early, making a 28-day batch duration sufficient, although a slow mechanism persists beyond 30 days. Thin-section experiments demonstrated that liquid-phase circulation is crucial; without it, Ni adsorption on intact rocks is significantly lower than on crushed samples. Microscopic and spectroscopic analyses confirmed adsorption primarily on clay minerals, with a new Ni-containing phase forming at the nanoscale. Competitive adsorption tests revealed that BCF has a higher affinity for Co(II) but a greater capacity for Ni(II). Through-diffusion modeling showed similar diffusion coefficients and capacity factors for both ions. The BCF exhibits favorable characteristics compared to other argillaceous formations, supporting its potential as a host rock for high-level radioactive waste repositories. These findings contribute to

understanding the retention behavior of clay minerals, highlighting the importance of experimental conditions and validating the use of the BCF for long-term containment.

Supplementary Materials: The following supporting information can be downloaded at <https://www.mdpi.com/article/10.3390/min14121299/s1>, Figure S1: Elemental maps acquired using laboratory micro-XRF; Figure S2: Correlation matrix with scatter plots of elemental intensities from μ -XRF mapping; Figure S3: Through-diffusion experiments: experimental data and model results of the outlet reservoir; Table S1: Composition of the Boda synthetic porewater.

Author Contributions: Conceptualization, O.C., F.S. and J.O.; methodology, O.C., F.S., M.A. and J.O.; investigation, O.C., F.S., M.F., T.K., Z.F., D.Z., M.A. and J.O.; writing—original draft preparation, O.C., T.K. and D.Z.; writing—review and editing, M.F., M.A. and J.O.; funding acquisition, J.O. All authors have read and agreed to the published version of the manuscript.

Funding: The research was supported by the European Joint Programme on Radioactive Waste Management (EURAD and EURAD-2) co-funded by the European Union through the EURATOM Programme (EU grant agreement Nos. 847593 and 101166718) and by the Elettra Sincrotrone Trieste under the IUS internal project (Elettra Nos. 20215774 and 20220423). This research was supported by grant No. VEKOP-2.3.3-15-2016-00002 from the European Structural and Investment Funds.

Data Availability Statement: The data related to the present study can be obtained from the corresponding author, J. Osan (osan.janos@ek.hun-ren.hu), upon personal request.

Acknowledgments: We acknowledge Elettra Sincrotrone Trieste for providing access to its synchrotron radiation facilities and acknowledge the staff of the XRF beamline for their assistance in data collection. We also thank the Helmholtz-Zentrum Berlin für Materialien und Energie for the allocation of synchrotron radiation beamtime. The courtesy of the Public Limited Company for Radioactive Waste Management (PURAM, Hungary) for providing the samples for analysis is also appreciated. We are grateful to Liesbeth Van Laer for her comments and suggestions that have greatly increased the quality of this paper.

Conflicts of Interest: The authors declare no conflicts of interest.

References

1. Dähn, R.; Scheidegger, A.M.; Manceau, A.; Curti, E.; Baeyens, B.; Bradbury, M.H.; Chateigner, D. Th Uptake on Montmorillonite: A Powder and Polarized Extended X-Ray Absorption Fine Structure (EXAFS) Study. *J. Colloid Interface Sci.* **2002**, *249*, 8–21. [[CrossRef](#)]
2. Osán, J.; Kéri, A.; Breitenner, D.; Fábrián, M.; Dähn, R.; Simon, R.; Török, S. Microscale Analysis of Metal Uptake by Argillaceous Rocks Using Positive Matrix Factorization of Microscopic X-Ray Fluorescence Elemental Maps. *Spectrochim. Acta Part B At. Spectrosc.* **2014**, *91*, 12–23. [[CrossRef](#)]
3. Tertre, E.; Dazas, B.; Asaad, A.; Ferrage, E.; Grégoire, B.; Hubert, F.; Delville, A.; Delay, F. Connecting Molecular Simulations and Laboratory Experiments for the Study of Time-Resolved Cation-Exchange Process in the Interlayer of Swelling Clay Minerals. *Appl. Clay Sci.* **2021**, *200*, 105913. [[CrossRef](#)]
4. Dähn, R.; Jullien, M.; Scheidegger, A.M.; Poinssot, C.; Baeyens, B.; Bradbury, M.H. Identification of Neoformed Ni-Phyllosilicated upon Ni Uptake in Montmorillonite: A Transmission Electron Microscopy and Extended X-Ray Absorption Fine Structure Study. *Clays Clay Miner.* **2006**, *54*, 209–219. [[CrossRef](#)]
5. Marques Fernandes, M.; Vér, N.; Baeyens, B. Predicting the Uptake of Cs, Co, Ni, Eu, Th and U on Argillaceous Rocks Using Sorption Models for Illite. *Appl. Geochem.* **2015**, *59*, 189–199. [[CrossRef](#)]
6. Chen, Z.; Montavon, G.; Guo, Z.; Wang, X.; Razafindratsima, S.; Robinet, J.C.; Landesman, C. Approaches to Surface Complexation Modeling of Ni(II) on Callovo-Oxfordian Clayrock. *Appl. Clay Sci.* **2014**, *101*, 369–380. [[CrossRef](#)]
7. Dähn, R.; Baeyens, B.; Fernandes, M.M. Zn Uptake by Illite and Argillaceous Rocks. *Geochim. Cosmochim. Acta* **2021**, *312*, 180–193. [[CrossRef](#)]
8. Fedor, F.; Máthé, Z.; Ács, P.; Koroncz, P. New Results of Boda Claystone Research: Genesis, Mineralogy, Geochemistry, Petrophysics. *Geol. Soc. Lond. Spec. Publ.* **2019**, *482*, 75–92. [[CrossRef](#)]
9. Nuclear Energy Agency (NEA). *Clay Club Catalogue of Characteristics of Argillaceous Rocks*; OECD NEA: Boulogne-Billancourt, France, 2022.
10. Sámson, M. (Ed.) *Final Report of Borehole BAF-2. (In Hungarian) RHK-N-011/14*; PURAM Ltd.: Paks, Hungary, 2015.
11. Mell, P.; Megyeri, J.; Riess, L.; Máthé, Z.; Hámos, G.; Lázár, K. Diffusion of Sr, Cs, Co and I in Argillaceous Rock as Studied by Radiotracers. *J. Radioanal. Nucl. Chem.* **2006**, *268*, 411–417. [[CrossRef](#)]
12. Gergely, F.; Osán, J.; Szabó, B.K.; Török, S. Analytical Performance of a Versatile Laboratory Microscopic X-Ray Fluorescence System for Metal Uptake Studies on Argillaceous Rocks. *Spectrochim. Acta Part B At. Spectrosc.* **2016**, *116*, 75–84. [[CrossRef](#)]

13. Lázár, K.; Máthé, Z.; Németh, T.; Kovács-Kis, V.; Stichleutner, S.; Kovács, I. Iron-Bearing Minerals in the Boda Claystone Formation: Correspondences with Stages of Evolution Revealed by Mössbauer Spectroscopy. *Minerals* **2024**, *14*, 196. [CrossRef]
14. Hrabovszki, E.; Tóth, E.; Tóth, T.M.; Máthé, Z.; Schubert, F. Potential Formation Mechanisms of Early Diagenetic Displacive Veins in the Permian Boda Claystone Formation. *J. Struct. Geol.* **2020**, *138*, 104098. [CrossRef]
15. Árkai, P.; Demény, A.; Fórizs, I.; Balogh, K.; Nagy, G.; Máthé, Z. Composition, Diagenetic and Post-Diagenetic Alterations of a Possible Radioactive Waste Repository Site: The Boda Albitic Claystone Formation, Southern Hungary. *Acta Geol. Hung.* **2000**, *43*, 351–378.
16. Lázár, K.; Máthé, Z.; Lázár, K.; Máthé, Z. Claystone as a Potential Host Rock for Nuclear Waste Storage. In *Clay Minerals in Nature-Their Characterization, Modification and Application*; IntechOpen: London, UK, 2012. [CrossRef]
17. Varga, A.; Szakmány, G.; Raucsik, B.; Máthé, Z. Chemical Composition, Provenance and Early Diagenetic Processes of Playa Lake Deposits from the Boda Siltstone Formation (Upper Permian), SW Hungary. *Acta Geol. Hung.* **2005**, *48*, 49–68. [CrossRef]
18. Sipos, P.; Németh, T.; Máthé, Z. Preliminary Results on the Co, Sr and Cs Sorption Properties of the Analcime-Containing Rock Type of the Boda Siltstone Formation. *Cent. Eur. Geol.* **2010**, *53*, 67–78. [CrossRef]
19. Varga, A.; Raucsik, B.; Szakmány, G.; Máthé, Z. Mineralogical, Petrological and Geochemical Characteristics of the Siliciclastic Rock Types of Boda Siltstone Formation. *Bull. Hung. Geol. Soc.* **2006**, *136*, 201–232.
20. Szabó, G.; Rell, P.; Osváth, S.; Valyon, J.; Bálint, M.; Máthé, Z. *Sorption Studies on BAF-2 Drilling Cores. (In Hungarian) RHK-N-021/16*; PURAM Ltd.: Paks, Hungary, 2017.
21. Breitner, D.; Osán, J.; Fábrián, M.; Zagyvai, P.; Szabó, C.; Dähn, R.; Marques Fernandes, M.; Sajó, I.E.; Máthé, Z.; Török, S. Characteristics of Uranium Uptake of Boda Claystone Formation as the Candidate Host Rock of High Level Radioactive Waste Repository in Hungary. *Environ. Earth Sci.* **2015**, *73*, 209–219. [CrossRef]
22. Czömpöly, O.; Fábrián, M.; Korányi, T.I.; Nagy, G.; Horváth, Z.E.; Zizak, I.; Pollastri, S.; Aertsens, M.; Osán, J. Adsorption and Diffusion of Selenite on Boda Claystone Formation. *Appl. Clay Sci.* **2023**, *241*, 106997. [CrossRef]
23. Bradbury, M.H.; Baeyens, B. A Physicochemical Characterisation and Geochemical Modelling Approach for Determining Porewater Chemistries in Argillaceous Rocks. *Geochim. Cosmochim. Acta* **1998**, *62*, 783–795. [CrossRef]
24. USGS-Description of Input and Examples for PHREEQC Version 3—A Computer Program for Speciation, Batch-Reaction, One-Dimensional Transport, and Inverse Geochemical Calculations. Available online: <https://pubs.usgs.gov/tm/06/a43/> (accessed on 9 December 2024).
25. Grivé, M.; Duro, L.; Colàs, E.; Giffaut, E. Thermodynamic Data Selection Applied to Radionuclides and Chemotoxic Elements: An Overview of the ThermoChimie-TDB. *Appl. Geochem.* **2015**, *55*, 85–94. [CrossRef]
26. Orucoglu, E.; Grangeon, S.; Gloter, A.; Robinet, J.C.; Madé, B.; Tournassat, C. Competitive Adsorption Processes at Clay Mineral Surfaces: A Coupled Experimental and Modeling Approach. *ACS Earth Space Chem.* **2022**, *6*, 144–159. [CrossRef]
27. Ver, N.; Baeyens, B.; Marques Fernandes, M.; Breitner, D. *Macroscopic Sorption Investigations on Argillaceous Rock Samples from the Boda Claystone Formation*; Hungarian Academy of Sciences Centre for Energy Research: Budapest, Hungary, 2012.
28. Rahman, M.S.; Clark, M.W.; Yee, L.H.; Comarmond, M.J.; Payne, T.E.; Burton, E.D. Effects of PH, Competing Ions and Aging on Arsenic(V) Sorption and Isotopic Exchange in Contaminated Soils. *Appl. Geochem.* **2019**, *105*, 114–124. [CrossRef]
29. Zizak, I. The MySpot Beamline at BESSY II. *J. Large-Scale Res. Facil. JLSRF* **2016**, *2*, A102. [CrossRef]
30. Karydas, A.G.; Czyzycki, M.; Leani, J.J.; Migliori, A.; Osán, J.; Bogovac, M.; Wrobel, P.; Vakula, N.; Padilla-Alvarez, R.; Menk, R.H.; et al. An IAEA Multi-Technique X-Ray Spectrometry Endstation at Elettra Sincrotrone Trieste: Benchmarking Results and Interdisciplinary Applications. *J. Synchrotron Radiat. I* **2018**, *25*, 189–203. [CrossRef] [PubMed]
31. Takeda, M.; Nakajima, H.; Zhang, M.; Hiratsuka, T. Laboratory Longitudinal Diffusion Tests: 1. Dimensionless Formulations and Validity of Simplified Solutions. *J. Contam. Hydrol.* **2008**, *97*, 117–134. [CrossRef]
32. Bradbury, M.H.; Baeyens, B. Sorption Modelling on Illite Part I: Titration Measurements and the Sorption of Ni, Co, Eu and Sn. *Geochim. Cosmochim. Acta* **2009**, *73*, 990–1003. [CrossRef]
33. Zhao, X.; Wang, Y.; Wu, H.; Fang, L.; Liang, J.; Fan, Q.; Li, P. Insights into the Effect of Humic Acid on Ni(II) Sorption Mechanism on Illite: Batch, XPS and EXAFS Investigations. *J. Mol. Liq.* **2017**, *248*, 1030–1038. [CrossRef]
34. Zhao, X.; Qiang, S.; Wu, H.; Yang, Y.; Shao, D.; Fang, L.; Liang, J.; Li, P.; Fan, Q. Exploring the Sorption Mechanism of Ni(II) on Illite: Batch Sorption, Modelling, EXAFS and Extraction Investigations. *Sci. Rep.* **2017**, *7*, 8495. [CrossRef] [PubMed]
35. Christiansen, B.; Torstenfelt, B. Diffusion of Nickel, Strontium, Iodine, Cesium and Americium in Loosely Compacted Bentonite at High PH. *Radiochim. Acta* **1988**, *44–45*, 219–224. [CrossRef]
36. García-Gutiérrez, M.; Cormenzana, J.L.; Missana, T.; Alonso, U.; Mingarro, M. Diffusion of Strongly Sorbing Cations (⁶⁰Co and ¹⁵²Eu) in Compacted FEBEX Bentonite. *Phys. Chem. Earth Parts A/B/C* **2011**, *36*, 1708–1713. [CrossRef]
37. García-Gutiérrez, M.; Cormenzana, J.L.; Missana, T.; Mingarro, M.; Alonso, U. Diffusion of ⁶⁰Co, ¹³⁷Cs and ¹⁵²Eu in Opalinus Clay. *MRS Proc.* **2008**, *1124*, 706. [CrossRef]

Disclaimer/Publisher’s Note: The statements, opinions and data contained in all publications are solely those of the individual author(s) and contributor(s) and not of MDPI and/or the editor(s). MDPI and/or the editor(s) disclaim responsibility for any injury to people or property resulting from any ideas, methods, instructions or products referred to in the content.